SWOT Data Assimilation with Correlated Error Reduction: Fitting Model and Error Together

Yu Gao, Sarah T. Gille, Bruce D. Cornuelle, Matthew R. Mazloff

Scripps Institution of Oceanography, University of California, San Diego, 9500 Gilman Drive, La Jolla, CA, 92093, USA

This is a non-peer reviewed manuscript that was submitted to Journal of Atmospheric and Oceanic Technology, May 1, 2024

Corresponding author: Sarah Gille, sgille@ucsd.edu

ABSTRACT: The Surface Water Ocean Topography (SWOT) satellite mission provides high-resolution two-dimensional sea surface height (SSH) data with swath coverage. However, spatially correlated errors affect these SSH measurements, particularly in the cross-track direction. The scales of errors can be similar to the scales of ocean features. Conventionally, instrumental errors and ocean signals have been solved for independently in two stages. Here, we have developed a one-stage procedure that solves for the correlated error at the same time that data are assimilated into a dynamical ocean model. This uses the ocean dynamics to distinguish ocean signals from observation errors. We test its performance relative to the two-stage method using simplified dynamics and a data set consisting of westward propagating Rossby waves, along with correlated instrumental errors of varying magnitudes. In a series of ensemble analyses, we found that the one-stage approach consistently outperforms the two-stage approach when estimating SSH signal and correlated errors. The one-stage approach can recover over 95% of the SSH signal, while skill for the two-stage approach drops significantly as error increases. Our findings suggest that solving for the correlated errors within the assimilation framework can provide an effective analysis approach, reducing the risks of confounding signal and instrument noise.

SIGNIFICANCE STATEMENT: The Surface Water and Ocean Topography (SWOT) satellite measures sea surface height (SSH) with unprecedented spatial resolution. However, measured SSH can include large-scale errors associated with slowly varying spatial shifts in the orientation of the satellite antenna. This study introduces a methodology for correcting the large-scale errors in data assimilation problems. By fitting errors and ocean dynamical signals at the same time, we reduce uncertainties both in the signal and in the large-scale error.

1. Introduction

The Surface Water and Ocean Topography (SWOT) satellite, launched in December 2022, has ushered in a new era of high-resolution sea surface height (SSH) measurements, offering unparalleled coverage of the global ocean surface (Fu et al. 2012). The SWOT satellite uses the Ka-band Radar Interferometer (KaRin) to measure ocean and surface water levels over a 120-km wide swath with a near-nadir gap of approximately 20 km width (Fu et al. 2012; Fu and Ubelmann 2014; Esteban-Fernandez 2017; Morrow et al. 2019). With its high-resolution swath measurements, the SWOT satellite can measure the two-dimensional structure of small-scale features, facilitating the study of small-scale currents, tides, and oceanic circulation. However, these new measurement capabilities come with significant challenges, including both measurement noise and spatially correlated errors. Spatially correlated errors impact SWOT data, predominantly in the cross-track direction (Esteban-Fernandez 2017).

The SWOT error budget sets error requirements as a function of wavelength, making SWOT the first altimetric mission to do so (Esteban-Fernandez 2017). While SWOT's initial performance is reported to be excellent, the possibility of spatially correlated error and the large volume of data produced by the mission necessitate innovative methods (Gaultier et al. 2016; Dibarboure et al. 2022).

In advance of the satellite launch, Metref et al. (2019) proposed a strategy to reduce the spatially structured errors of the SWOT satellite mission's SSH data through a two-stage approach. The first stage involves detrending the SSH data by projecting them onto a subspace spanned by the SWOT spatially structured errors. The second stage uses the detrended measurements as inputs to a data assimilation scheme. Metref et al. (2020) found that the assimilation of SWOT data reduces the root-mean-square-error (RMSE) of the reconstructed SSH, relative vorticity, and surface currents and also improves the noise-to-signal ratio and spectral coherence of the SSH signal at the mesoscale. A limitation of the two-stage approach is that error and signal are not necessarily orthogonal. Any overlap between the assumed error structure and the actual signal can result in "leakage", leading to ocean signals being misrepresented as measurement errors (Dibarboure and Ubelmann 2014; Dibarboure et al. 2022). Despite this limitation, two-stage approaches represent traditional practice in satellite products and in assimilation, which treat error removal as a distinct quality-control step before data assimilation is used to infer properties of the ocean state.

In this study, we introduce a streamlined one-stage approach, extending the framework of Metref et al. (2020) while aiming to mitigate the ambiguity between correlated errors and ocean signals. Our one-stage approach directly integrates the reduction of correlated SWOT errors into the SSH estimation process, merging the two stages of Metref et al. (2019, 2020). In addition to minimizing the risk of confounding genuine ocean signals with correlated errors, our method allows us to consider temporal correlation of SWOT geometric and orientation errors and to incorporate an estimation of wet troposphere contamination.

In order to develop our one-stage approach we work with an idealized testbed scenario, centered in the California Current region. The California Current System is a complex region, where sea level variability is influenced by both local winds and remote forcing forces from equatorial winds. In this case, our input data are SSH Anomalies (SSHA), simplified to contain only wave-like disturbances, roughly consistent with westward propagating Rossby waves (Watanabe et al. 2016). These input data capture the dominant SSHA variability in mid-latitude regions such as the California Current System (e.g. Chelton and Schlax 1996; Ivanov et al. 2010; Todd et al. 2011; Farrar et al. 2021; Gómez-Valdivia et al. 2017), although formally observed SSHA features are more consistent with westward propagating nonlinear vortices rather than Rossby waves (Chelton et al. 2007, 2011). The westward propagation speed for SSHA features depends on latitude and stratification and is typically around 1° longitude in 50 days.

To demonstrate this methodology, we employ a quasi-geostrophic (QG) Rossby wave model, rather than a full general circulation model. The reduced Rossby wave model is able to capture leading-order ocean variability (Wakata and Kitaya 2002), in this case SSHA signals attributable to westward propagating Rossby waves. Within our simplified scenario, our goal is solve for correlated errors as well as dynamical variations in sea surface height, using either a one-stage or a two-stage approach, and to test the extent to which a one-stage method can ameliorate the "leakage" due to the ambiguity between ocean signal and correlated errors.

This paper is organized as follows: Section 2 (a) reviews the Bayesian estimation method that we employ, (b) describes our simplified ocean data set based on the idealized Rossby wave model, and (c) reviews our implementation of the correlated error model. Section 3 describes the one-stage versus two-stage approach in an idealized multi-day simulation for a single start date, and then reviews statistics for an ensemble of different case studies. Section 4 provides a discussion and conclusions.

2. Methodology

a. Bayesian estimation method

We employ a Bayesian estimation method, consistent with the approach outlined by Wunsch (1996). Here we provide a brief overview of this method, as formulated for SWOT correlated error reduction, adopting the notation used by Ide et al. (1997) and Kachelein et al. (2022) with some modifications.

A zero-mean SSHA sample is represented as a column vector $\mathbf{h}$ of length N, which satisfies the equation:

$$\mathbf{h} = \mathbf{H}\mathbf{a} + \mathbf{r}. \tag{1}$$

Here, $\mathbf{h}$ is treated as a correction to the background state, $\mathbf{H}$ represents the model basis functions, $\mathbf{a}$ represents the model parameters, and $\mathbf{r}$ is the residual. (Formally, Eq. 1 should be thought of as providing a correction to the all-zero model parameters that would be obtained if $\mathbf{h}$ exactly matched the background state.) The appendix provides a glossary to as a quick reference for the variables defined in this section. In this study, the elements of $\mathbf{H}$ are Rossby waves that are expressed as sines and cosines:

$$H_{i,n} = \cos(\mathbf{k}_n \cdot \mathbf{x}_i - \omega_n t_i) \tag{2}$$

$$H_{i,n+N_m} = \sin(\mathbf{k}_n \cdot \mathbf{x}_i - \omega_n t_i), \tag{3}$$

where $\mathbf{x}_i$ is a vector representing geographic position of the ith observation in Cartesian coordinates, t_i is the time of the observation, $\mathbf{k}_n$ is the vector representation of the nth wavenumber in the model basis, N_m is the number of waves, and ω_n is the frequency of the nth wavenumber. Each row of (1) can be expressed as

$$h_i = h(\mathbf{x}_i, t_i) = \sum_{n=1}^{N_m} [a_n H_{i,n} + a_{n+N_m} H_{i,n+N_m}] + r_i \tag{4}$$

where h_i denotes the ith SSHA observation, and we assume a total of N_d observations. In vector form $\mathbf{h}(\mathbf{x}, \mathbf{t})$ comprises a linear set of N_d equations, which represent the observations by N_m Rossby waves, and the matrix $\mathbf{H}$ has $N_d \times 2N_m$ elements. The amplitudes of the sinusoidal waves are a_n, where in vector form $\mathbf{a}$ is a $2N_m$-element vector.

The dispersion relation for Rossby waves defines the relationship between their frequency and wavenumber. For these waves on a β-plane, it is $\omega_n = -\beta k_n / (k_n^2 + l_n^2 + L_d^{-2})$, where ω_n represents the frequency of the n-th wave, k_n and l_n are zonal and meridional wavenumbers, respectively, and L_d is the Rossby radius of deformation. The meridional derivative of the Coriolis parameter, f, is $\beta = df/dy$, which is taken to be constant. The phase speed of the waves (ω_n/k_n) is westward due to the negative sign, and increases with increasing wavelength until the long wave limit where $k_n^2 + l_n^2 << L_d^{-2}$.

The depth-mean buoyancy frequency B influences the first baroclinic mode Rossby radius of deformation, described as:

$$L_d \sim \frac{BD}{\pi f}, \tag{5}$$

where D is the total depth of the water column, and B is stratification.The Rossby radius of deformation is larger in regions where the ocean is deep (larger D) or has strong stratification (larger B). To determine the buoyancy frequency, we used a representative stratification taken from a numerical simulation of the California Current region (Mazloff et al. 2020). The simulation provides detailed vertical profiles, capturing variations in temperature and salinity across the water column. From these simulated density profiles, the buoyancy frequency was calculated using the Brunt-Väisälä formula.

The unknown model parameters $\mathbf{a}$ are estimated as

$$\hat{\mathbf{a}} = \left(\mathbf{H}^T \mathbf{R}^{-1} \mathbf{H} + \mathbf{P}^{-1}\right)^{-1} \mathbf{H}^T \mathbf{R}^{-1} \mathbf{h}. \tag{6}$$

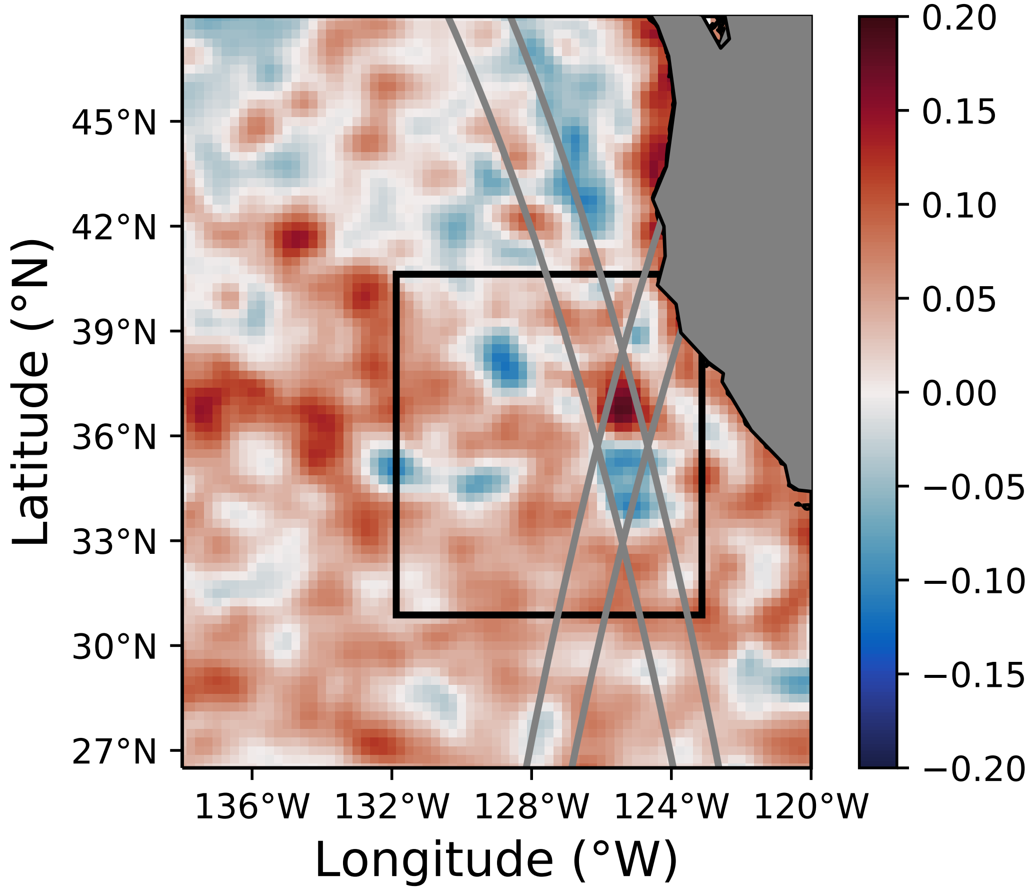

FIG. 1. a) Sea Surface Height (SSH) anomalies in the California Current region on 1 January 2016. Black lines indicate the 10° latitude by 9° longitude region of interest for this study, and gray lines indicate the SWOT ground tracks along the California Coast.

This solution minimizes both the model misfit and the magnitudes of the model parameters. The posterior covariance matrix of the difference between the estimated and true model parameters is

$$\langle(\mathbf{a}-\hat{\mathbf{a}})(\mathbf{a}-\hat{\mathbf{a}})^{\mathrm{T}}\rangle = \left(\mathbf{H}^{\mathrm{T}}\mathbf{R}^{-1}\mathbf{H}+\mathbf{P}^{-1}\right)^{-1}, \tag{7}$$

where $\mathbf{R}$ is an $N_d \times N_d$ matrix representing the error covariance of the observations, and $\mathbf{P}$ is an $2N_m \times 2N_m$ matrix representing the a priori error covariance of the model elements $\mathbf{a}$.

Although the inversion of the matrix $\left(\mathbf{H}^T\mathbf{R}^{-1}\mathbf{H}+\mathbf{P}^{-1}\right)$ takes place in the model space (dimensioned $2N_m \times 2N_m$), the $\mathbf{R}$ matrix is $N_d \times N_d$, which makes it expensive to invert unless it is diagonal. Here we simplify further by defining $\mathbf{R}$ to be a multiple of the identity matrix.

If $\mathbf{R} = \sigma_d^2\mathbf{I}$, where σ_d is the standard deviation of the measurement (data) noise, then (6) simplifies to

$$\hat{\mathbf{a}} = \left(\mathbf{H}^T\mathbf{H} + \sigma_d^2\mathbf{P}^{-1}\right)^{-1}\mathbf{H}^T\mathbf{h}, \tag{8}$$

which is all in the model space. The diagonal of the matrix $\mathbf{P}$ is defined as $\left(\sqrt{k^2+l^2}\right)^{-2}$, where k and l are respectively the zonal and meridional components of wavenumber $\mathbf{k}$. The diagonal of $\sigma_d^2\mathbf{P}^{-1}$ is the noise-to-signal ratio. Larger values imply more noise relative to information and lead to solutions that are closer to the prior guess of zero.

The posterior uncertainty covariance (7) can be transformed to physical space by pre- and post-multiplying by a matrix $\mathbf{H}_{map}$ that converts from $\mathbf{a}$ to either the swath or the mapping grid:

$$\langle(\mathbf{h}_{map} - \widehat{\mathbf{h}_{map}})(\mathbf{h}_{map} - \widehat{\mathbf{h}_{map}})^{\mathrm{T}}\rangle = \mathbf{H}_{map}\left(\mathbf{H}^{\mathrm{T}}\mathbf{R}^{-1}\mathbf{H}+\mathbf{P}^{-1}\right)^{-1}\mathbf{H}_{map}{}^{\mathrm{T}}. \tag{9}$$

The mapping matrix, $\mathbf{H}_{map}$, can be defined for any set of space–time points. For example, the time of the map can be set to the beginning, middle, or end of the assimilation time range, or any time in the past or future. Although (9) produces a full uncertainty covariance matrix, the general practice is to report only the diagonal elements or the largest eigenvalues and eigenvectors of this matrix, which represent the largest orthogonal modes of posterior uncertainty.

b. Simplified Rossby wave model

To develop an approach for analyzing propagating waves as well as correlated satellite error, we start with a simplified data set that contains realistic sea surface height variability and for which the model parameters are fully known. To achieve this we use daily altimeter fields, mapped to a 0.25° grid, within the region shown in Figure 1, with data from the Copernicus Global Ocean Gridded L4 Sea Surface Heights And Derived Variables Reprocessed dataset (Copernicus Marine Service Information 2023).

In the discussion that follows, we use L4 gridded SSHA fields starting January 1, 2016 through early 2017. We show case-study results and assess their robustness by using a 12-member ensemble with starting on the first day of each month. In all cases, we consider 80-day records: a 40-day period to estimate model parameters followed by a 40-day prediction period. For each member of the ensemble, the initial data set, here identified as $\mathbf{h}_{orig}$ is organized on a grid that contains 40 points in longitude and 36 points in latitude, so in the initial analysis, the number of gridded data points N_g will be 1440 data points per day, making the total number of observations over 40 days, $N_d = N_g \times 40$.

For each start date, we project a 40-day sequence of daily fields onto a basis set of 190 waves with properties typical of Rossby waves—190 cosine components and 190 sine components—meaning that in this implementation $N_m = 190$. The wavelengths include 10 zonal modes (0 to 5.1 cycles per degree in space) and 19 meridional modes (-5.24 to + 5.04 cycles per degree latitude), in both cases evenly incremented at intervals of 0.571 radians per degree (1 cycle in 11 degrees). In contrast with classic Fourier transforms, here the modes are chosen to include wavelengths slightly larger than the domain size to avoid periodicity within the space and time domain of the simulation. The meridional wavenumbers are asymmetric in the positive and negative directions to avoid having a large number of modes with wavenumber zero.

By construction, this basis set is not orthogonal over our test region, which would pose problems due to rank deficiency if we were not using the regularized inverse with $\mathbf{P}$ covariance matrices. The use of a non-orthogonal basis set is by design in order to capture low-wavenumber structures that are larger than our study domain.

Using this set of wavenumbers, we estimate model coefficients $\hat{\mathbf{a}}_{orig}$ that represent about 95% of the SSHA variance in the domain during the 40-day fitting period starting January 1, 2016 (Figure 2). We use $\hat{\mathbf{a}}_{orig}$ in the wave model to project SSHA forward in time, computing an estimated SSHA $\hat{\mathbf{h}}_{orig}$, as a function of time both for the fitting period and for 40 days afterward. At the mid-point of the 40-day fitting period, Figure 2 shows the original SSHA on 21 January 2016 (panel a), the fitted SSHA (panel b), and the residual difference $(\hat{\mathbf{h}}_{orig} - \mathbf{h}_{orig})$ (panel c).

The success of the fitting is largely due to the fact that the wave coefficients allow SSHA to propagate westward, as illustrated in the Hovmöller diagram in Figure 3, which shows the original SSHA data (panel a), the Rossby wave fit (panel b), and the difference between the SSHA data and Rossby wave fit (panel c) both for the fitting period (days 1–40) and for the prediction (days 40–80).

We repeated this fitting procedure 12 times, starting at the first day of each month of 2016. On average, the propagating Rossby wave model represents 70–90% of the SSHA variance over the 40-day fitting period, as illustrated in Figure 4 for the ensemble of 12 time periods. The fitting period is the first 40 days, to the left of the vertical dashed line. Gray lines show individual cases, and the red line is the ensemble mean. As a baseline measure, we compare the Rossby wave model with a null hypothesis prediction that the SSHA is constant, pegged at conditions on the 21st day (blue line). Over the 40-day fitting period, on average the Rossby wave model explains a higher fraction of variance (also known as the "skill") than does persistence (blue line), except within ±5 days on either side of day 21.

After the 40-day fitting period (right of the vertical dashed line in Figure 4), the skill of the Rossby wave model varies considerably, as indicated by the spread of the gray lines: in some cases the Rossby wave model continues to explain a large fraction of the gridded SSHA data, and in other cases the model diverges significantly. Differences could arise for a number of reasons: the Rossby wave model could omit frequency–wavenumber combinations that are important at some times, the system could experience occasional external forcing (e.g. from wind) that excites new propagating waves, the waves could propagate at speeds that differ from the linear Rossby wave phase speed (Chelton et al. 2007, 2011), or the model could be incomplete for other reasons. The skill decreases slightly less steeply for the Rossby wave model (red) than for persistence (blue), indicating that the Rossby wave model carries some useful information about the evolution of the SSHA field. The objective of this paper is focused on demonstrating the feasibility of including correlated error corrections within a model, and we leave for other studies the possibility of carrying out more detailed exploration of Rossby wave or QG representations of altimeter data.

The estimate $\hat{\mathbf{h}}_{orig}$ has the virtue of possessing perfectly known model coefficients, $\hat{\mathbf{a}}_{orig}$. Since our analysis requires a simplified data set with known model parameters, for the remainder of this paper we will use these estimated fields as the model truth. We define

$$\mathbf{h} = \hat{\mathbf{h}}_{orig} \tag{10}$$

$$\mathbf{a} = \hat{\mathbf{a}}_{orig}. \tag{11}$$

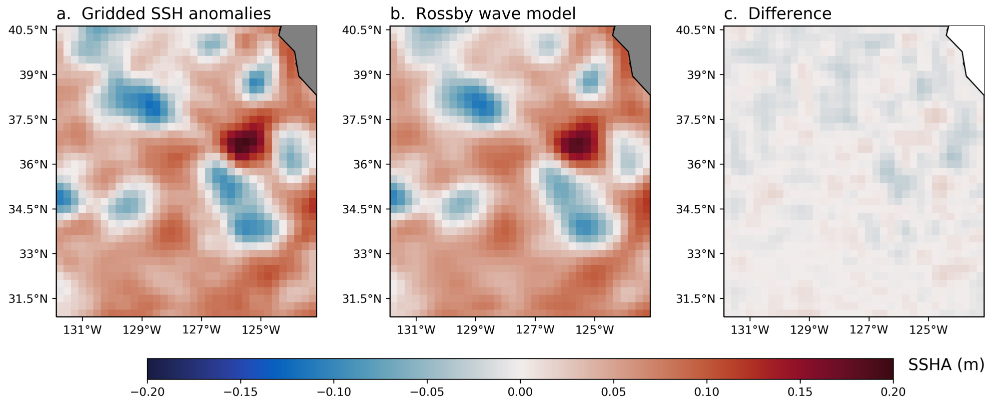

FIG. 2. a) SSHA from 21 January 2016, the mid-point of the fitting period for the analysis beginning on 1 January 2016. b) SSHA represented by 190 Rossby waves; c) residual difference, corresponding to about 3.1% of the variance on this date.

Using only measurements collected along the SWOT satellite swath, our objective will be to evaluate how well we can find appropriate wave coefficients **a** and replicate the full SSHA field **h**, both during the fitting period and projecting forward in time.

We subsample the simplified SSHA field **h** only within the SWOT swath, which is approximately 120 km wide. Because the Rossby waves have a large spatial structure, we subsample the SWOT data grid, using every 8th point in the cross-track direction and every 16th row in the along-track direction. For the SWOT one-day repeat period, carried out from April–July 2023, each day yields approximately 225 points from ascending satellite passes and 225 points from descending satellite passes, mimicking the SWOT satellite sampling. To these in-swath SSHA points we add simulated satellite sampling errors, as discussed in the next section.

c. Correlated error model

Following Metref et al. (2020) and Esteban-Fernandez (2017), our correlated error reduction procedure considers four error terms, defined by seven (unknown) coefficients, α_i. Timing error α_0, is treated as a constant and is attributed to instrument timing drift. Roll error, expressed as $\alpha_1 x_c$, results from the satellite's roll angle and is assumed to increase linearly in the cross-track coordinate relative to nadir, x_c. The baseline dilation error, $\alpha_2 x_c^2$, originates from variations in the satellite mast length. Lastly, the phase error results from relative variations in phase between the satellite's left and right antennas, leading to distinct cross-track linear errors in each half swath.

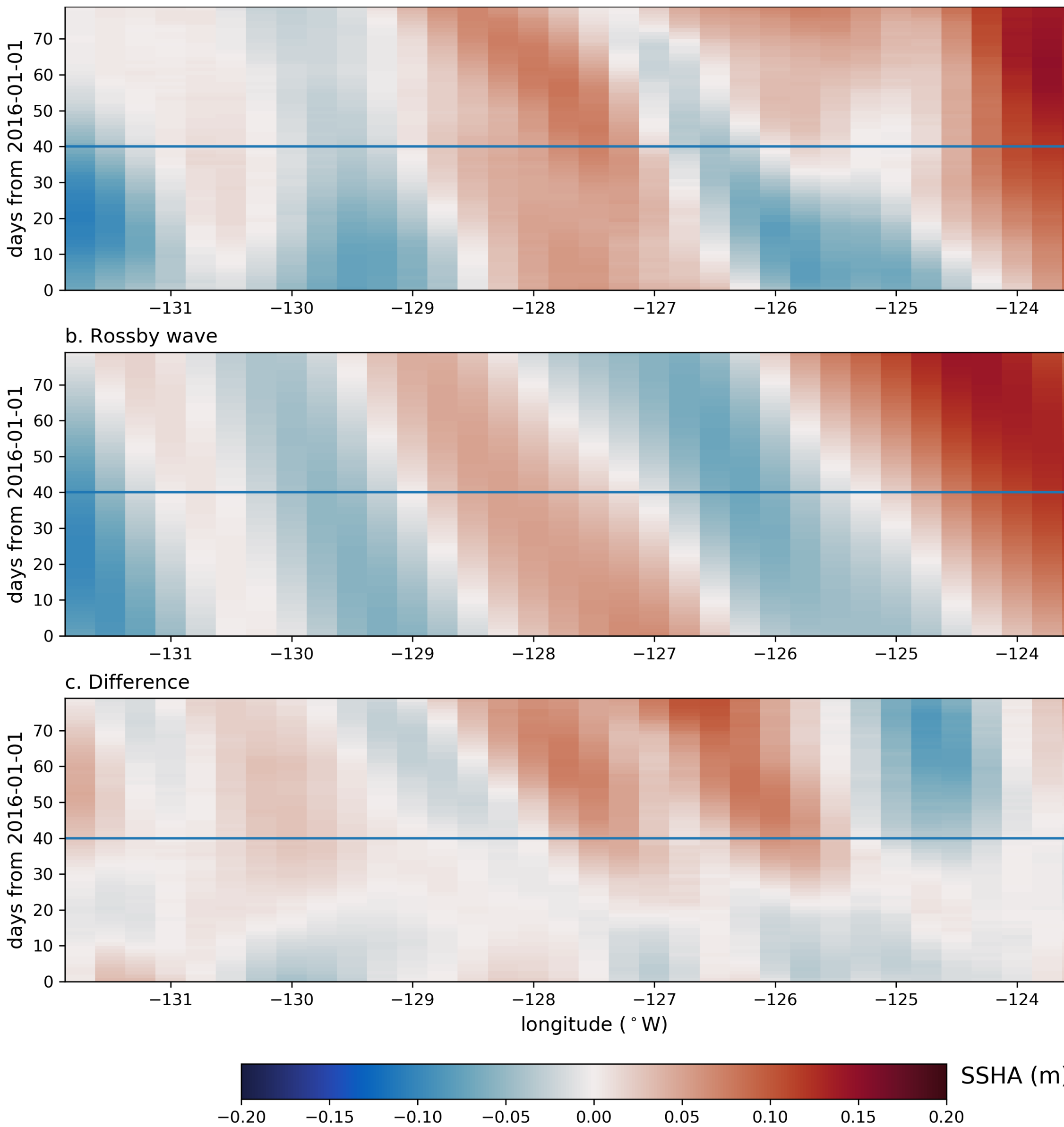

Fig. 3. Sea Surface Height Anomalies (SSHA) (a) SSHA from Copernicus gridded fields (sometimes referred to as AVISO) at 34.625°N latitude, (b) smoothed version of SSHA created by projecting gridded Copernicus SSHA values onto a set of 190 wave modes consistent with large-scale Rossby waves, (c) difference between original and smoothed SSHA data.

This is represented using Heaviside functions, $\mathcal{H}(x)$, which equal 1 when $x \geq 0$ and 0 otherwise:

$[\alpha_3+\alpha_4 x_c]\mathcal{H}(-x_c)+[\alpha_5+\alpha_6 x_c]\mathcal{H}(x_c)$. Together the total error is modeled as:

$$e_{\text{total}} = \alpha_0+\alpha_1 x_c+\alpha_2 x_c^2+[\alpha_3+\alpha_4 x_c]\mathcal{H}(-x_c)+[\alpha_5+\alpha_6 x_c]\mathcal{H}(x_c), \tag{12}$$

Following the approach of Metref et al. (2019), we assume that within our relatively small domain, the coefficients remain constant along each pass along the track. In other words, we assume that the spatial decorrelation scale of the along-track error exceeds our domain size. Mathematically, the terms represented by α_0 and α_1 are redundant with the inclusion of Heaviside functions for the left and right swath, which will lead to a rank deficient matrix. In this case, since we use a regularized inverse, we retain all of the terms proposed by Metref et al. (2019). The prior covariance matrix $\mathbf{P}$ sets the expected relative sizes of the full swath adjustments represented by α_0 and α_1 and the left and right adjustments represented by α_3, α_4, α_5, and α_6.

In matrix form, for satellite pass m, the error model can be written:

$$\mathbf{e}_{total_m} = \mathbf{H}_{err_m}\mathbf{a}_{err_m}, \tag{13}$$

where vector $\mathbf{e}_{total_m}$ has N_s elements corresponding to each observation within the swath, and $\mathbf{H}_{err_m}$ is an $N_s\times 7$ matrix:

$$\mathbf{H}_{err_\mathbf{m}} = \begin{bmatrix} 1 & x_{c_1} & x_{c_1}^2 & \mathcal{H}(-x_{c_1}) & x_{c_1}\mathcal{H}(-x_{c_1}) & \mathcal{H}(x_{c_1}) & x_{c_1}\mathcal{H}(x_{c_1}) \\ \vdots & \vdots & \vdots & \vdots & \vdots & \vdots & \vdots \\ 1 & x_{c_i} & x_{c_i}^2 & \mathcal{H}(-x_{c_i}) & x_{c_i}\mathcal{H}(-x_{c_i}) & \mathcal{H}(x_{c_i}) & x_{c_i}\mathcal{H}(x_{c_i}) \\ \vdots & \vdots & \vdots & \vdots & \vdots & \vdots & \vdots \\ 1 & x_{c_{N_s}} & x_{c_{N_s}}^2 & \mathcal{H}(-x_{c_{N_s}}) & x_{c_{N_s}}\mathcal{H}(-x_{c_{N_s}}) & \mathcal{H}(x_{c_{N_s}}) & x_{c_{N_s}}\mathcal{H}(x_{c_{N_s}}) \end{bmatrix}, \tag{14}$$

where x_{c_i} refers to the ith element of a cross-track position x_c. The corresponding fitted parameters are

$$\mathbf{a}_{err_m} = \begin{bmatrix} \alpha_{0_m} & \alpha_{1_m} & \alpha_{2_m} & \alpha_{3_m} & \alpha_{4_m} & \alpha_{5_m} & \alpha_{6_m} \end{bmatrix}^T. \tag{15}$$

Since the error evolves in time, the error vectors are concatenated, and the error matrix is augmented to represent each ascending or descending satellite pass, which are assumed to have the same sampling on every pass, for a total of M passes, this results in a block diagonal matrix consisting of one $N_s \times 7$ matrix per satellite pass:

$$\mathbf{H}_{err} = \begin{bmatrix} \mathbf{H}_{err_1} & \mathbf{0} & \cdots & \mathbf{0} \\ \mathbf{0} & \mathbf{H}_{err_2} & \cdots & \mathbf{0} \\ \vdots & \vdots & \ddots & \vdots \\ \mathbf{0} & \mathbf{0} & \cdots & \mathbf{H}_{err_\mathbf{M}} \end{bmatrix} \quad (16)$$

$$\mathbf{a}_{err} = \begin{bmatrix} \mathbf{a}_{err_1} \\ \mathbf{a}_{err_2} \\ \vdots \\ \mathbf{a}_{err_\mathbf{M}} \end{bmatrix}. \quad (17)$$

The total number of data points N_d (and rows in $\mathbf{H}$) is thus $N_s \times M$.

Further errors in SWOT data could stem from a range of environmental corrections, including both uncorrelated noise and large-scale correlated signals. Among the possible large-scale errors is the mean dynamic topography (MDT). Total SSH required for data assimilation makes use of SSHA computed relative to the time-averaged measured mean sea surface. SSHA values are added to the estimated MDT to infer total dynamic topography. While the accuracy of the MDT is an ongoing challenge (e.g. Mazloff et al. 2014), for this proof-of-concept study we have bypassed the issue by considering only SSHA.

1) Two-stage approach

The first stage of the two-stage approach is error removal. Following (Metref et al. 2019), we consider only data collected within satellite swaths, here identified as $\mathbf{h}_{swath}$. To remove the correlated errors from the signal, in the two-stage approach we calculate the projection of $\mathbf{h}_{swath}$ onto the subspace spanned by the modeled errors in equation (12), minimizing the cost function:

$$\mathcal{J}_1(\mathbf{a}_{err}) = (\mathbf{h}_{swath} - \mathbf{H}_{err}\mathbf{a}_{err})^T \mathbf{R}^{-1} (\mathbf{h}_{swath} - \mathbf{H}_{err}\mathbf{a}_{err}) + \mathbf{a}_{err}^T \mathbf{P}_{err}^{-1} \mathbf{a}_{err}, \quad (18)$$

where $\mathcal{J}_1$ is a scalar representing the squared misfit between the data and the fitted error, summed over all N_s data points within the swath and over all M satellite passes included in the analysis, weighted by the data covariance $\mathbf{R}$, with $\mathbf{a}_{err}$ representing the modeled best estimate of the error

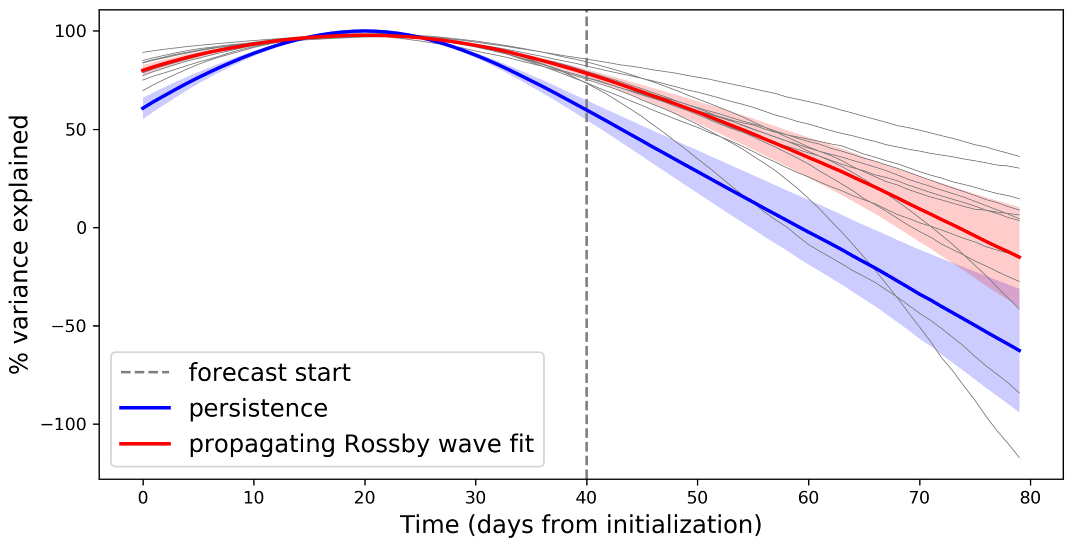

Fig. 4. Fraction of gridded Copernicus SSHA variance explained by the Rossby wave model as a function of day for an ensemble of 12 start dates, beginning the first of each month in 2016. Gray lines indicate individual realizations, the red line shows the mean, and red shading indicates twice the standard error of the mean ($2\sigma/\sqrt{12}$, where σ is the standard deviation of the 12 monthly realizations. Data from the first 40 days are used in the least-squares fitting procedure (to the left of the vertical dashed gray line). After 40 days, SSHA is predicted based only on information from the first 40 days. The blue line indicates persistence from the mid-point of the fitting period (day 21), with shading indicating twice the standard error of the mean.

parameters. The term $\mathbf{a}_{err}^T \mathbf{P}_{err}^{-1} \mathbf{a}_{err}$ imposes an additional constraint to prevent $\mathbf{a}_{err}$ from becoming large relative to the prior model covariance for the error terms, $\mathbf{P}_{err}$. We then define a proxy version of the SSHA data, $\tilde{\mathbf{h}}_{swath}$ as the difference between the SWOT signal $\mathbf{h}_{swath}$ and the projection onto $\mathbf{H}_{err}$ in vector form:

$$\tilde{\mathbf{h}}_{swath} = \mathbf{h}_{swath} - \mathbf{H}_{err} \hat{\mathbf{a}}_{err}. \tag{19}$$

The second stage of the two-stage approach is solving for sea surface height. We fit the difference $\tilde{\mathbf{h}}_{swath}$ to the subspace spanned by the Rossby wave model given by equations (2) and (3). This is applicable to all N_s data points within each swath and for all M time samples used in the fitting period.

$$\mathcal{J}_2 (\mathbf{a}_w) = (\tilde{\mathbf{h}}_{swath} - \mathbf{H}_{swath} \mathbf{a}_w)^T \mathbf{R}^{-1} (\tilde{\mathbf{h}}_{swath} - \mathbf{H}_{swath} \mathbf{a}_w) + \mathbf{a}_w^T \mathbf{P}^{-1} \mathbf{a}_w. \tag{20}$$

The $\mathbf{H}_{swath}$ matrix is the representation of (2) and (3) for data points within the swath only:

$$\mathbf{H}_{swath} = \begin{bmatrix} H_{1,1} & H_{1,2} & \cdots & H_{1,N_m} & H_{1,N_m+1} & \cdots & H_{1,2N_m} \\ \vdots & \vdots & \ddots & \vdots & \vdots & \ddots & \vdots \\ H_{MN_s,1} & H_{MN_s,2} & \cdots & H_{MN_s,N_m} & H_{MN_s,N_m+1} & \cdots & H_{MN_s,2N_m} \end{bmatrix}. \tag{21}$$

The true wave parameters are:

$$\mathbf{a}_w = \begin{bmatrix} a_1 & a_2 & \ldots & a_{N_m} & a_{N_m+1} & \ldots & a_{2N_m} \end{bmatrix}^T, \tag{22}$$

the estimated wave parameters are $\hat{\mathbf{a}}_w$, and $\mathbf{P}$ represents covariance matrix corresponding to the wave solutions. Using these estimates, we can find estimated values of SSHA both in the swath ($\hat{\mathbf{h}}_{swath}$) and throughout the full domain ($\hat{\mathbf{h}}$).

2) One-stage approach

The one-stage approach combines the error projection in (18) and SSHA model fit in (20) and solves for errors and SSHA signals simultaneously. We achieve this using an augmented matrix $\mathbf{H}_{total}$ that combines $\mathbf{H}_w$ and $\mathbf{H}_{err}$ together with an augmented parameter vector $\mathbf{a}_{total}$:

$$\mathbf{H}_{total} = [\mathbf{H}_{swath} | \mathbf{H}_{err}] \tag{23}$$

$$\mathbf{a}_{total} = \begin{bmatrix} \mathbf{a}_w \\ \mathbf{a}_{err} \end{bmatrix}. \tag{24}$$

The analysis minimizes the cost function:

$$\mathcal{J}(\mathbf{a}_{total}) = (\mathbf{h}_{swath} - \mathbf{H}_{total}\,\mathbf{a}_{total})^T \mathbf{R}^{-1} (\mathbf{h}_{swath} - \mathbf{H}_{total}\,\mathbf{a}_{total}) + \mathbf{a}_{total}^T \mathbf{P}_{total}^{-1} \mathbf{a}_{total}, \tag{25}$$

again where $\mathbf{a}_{total}^T \mathbf{P}_{total}^{-1} \mathbf{a}_{total}$ is the regularization term that prevents the model parameters from becoming large relative to their prior estimates. The portion of $\mathbf{a}_{total}$ representing the waves is $\mathbf{a}_w$ with $\hat{\mathbf{a}}_w$ representing the best estimate. This determines the time evolving wave-related SSHA within the swath, $\hat{\mathbf{h}}_{swath} = \mathbf{H}_{swath}\hat{\mathbf{a}}_w$, or over the full domain: $\hat{\mathbf{h}} = \mathbf{H}\hat{\mathbf{a}}_w$.

3) Experiment setup

In the experiments that follow, we apply both the one-stage approach and the two-stage approach to the ensemble of sea surface height data sets. For each ascending or descending satellite pass, the 7 separate SWOT correlated error parameters are drawn at random from a Gaussian distribution.

3. Results

1) Case study: One-stage versus two-stage approach

We first consider a case study, starting 1 January 2016. We apply the one-stage and two-stage correlated error reduction procedures to 40 days of synthetic satellite data and then use the estimated model parameters to make 40-day forecasts. We consider the SWOT satellite calibration/validation orbit, which uses a one-day repeat, meaning that 40 days of observations correspond to 80 separate satellite passes: 40 ascending passes and 40 descending passes. The model–data misfit is measured by the normalized mean squared error (NMSE):

$$\mathrm{NMSE} = \frac{\mathrm{mean}\left((\mathbf{h}_{swath} - \hat{\mathbf{h}}_{swath})^2\right)}{\mathrm{mean}\left(\mathbf{h}^2_{swath}\right)} \tag{26}$$

where $\mathbf{h}_{swath}$ is the truth (i.e. the synthetic satellite data) and $\hat{\mathbf{h}}_{swath}$ is our estimate. NMSE quantifies how much the estimated values deviate from the true values, relative to the variance of those values. The percentage of variance explained, $100 \times (1 - \mathrm{NMSE})$ is a useful metric for assessing the performance of a model and reflects the proportion of the total variance in the observed data that the model successfully captures.

Within the SWOT swath, we compare the performance of the one-stage and two-stage approaches, evaluating results in a one-day snapshot mid-way through the training period. For this case study, the error components (i.e. the true $\mathbf{a}_{err}$) that together determine the correlated error were drawn from a random distribution, scaled such that when the terms are summed, the standard deviation of the correlated error is 34% of the SSHA standard deviation. This magnitude was also reflected in the σ_d and $\mathbf{P}$ error covariance prescribed in the model. In this example for the 40-day fitting period, the one-stage data assimilation approach effectively recovers over 99% of the SSHA variance on the satellite swath (Fig. 5c), while the two-stage approach removes correlated errors less effectively, recovering only 66% of the SSHA signal (Fig. 5e). For the correlated error, the one-stage approach successfully recovers 93.5% of the true error (Fig. 5h), while the two-stage approach demonstrates no skill in estimating errors (Fig. 5j). Differences are less pronounced when we consider the skill at reconstructing total SSHA ($\mathbf{h}+\mathbf{e}$): both approaches recover more than 99% of $\mathbf{h}+\mathbf{e}$ (Fig. 5m,o), implying that the shortcomings in the two-stage approach represent a failure to distinguish correlated errors from SSHA signal. The superior performance of the one-stage approach suggests that solving for correlated errors as part of the assimilation is more effective than implementing separate procedures to solve for correlated errors and propagating dynamical SSHA signals, since the slow propagation of the Rossby waves provides key information that allows them to be separated from correlated error.

Outside the satellite swath, the Rossby wave model provides a dynamical framework, allowing information measured by the satellite to propagate beyond the swath boundaries, filling in the full study domain. In the case study considered here, the one-stage approach shows better skill outside of the swath, with 62% of variance explained over the entire domain for the 40-day training period (Fig. 6b) compared with 29% in the two-stage approach (Fig. 6e). The two-stage approach also shows significant errors at the swath edges due to misinterpretation of error signals (see Fig. 6 e-f). To quantify the results more completely, in the next section we consider statistics based on an ensemble of model start dates.

2) Ensemble analysis

We now extend the case study to consider the ensemble of 12 start dates and a range of 30 different noise levels. For simplicity, for each noise level, we use a single value to set the standard deviation of each of the seven coefficients α_i that define the correlated error in (12), even though the coefficients have different units. We use a total of 30 different noise values, evenly spaced between 5×10^{-4} to 2.95×10^{-2}. These values lead to total correlated error perturbations of 3 cm or less. Results show that on average the one-stage approach outperforms the two-stage approach (Fig. 7a). When the over all error is small relative to the signal (i.e. the ratio of root-mean-squared error to root-mean-squared SSHA, RMSE/RMS_SSHA $\lesssim 0.05$), there is little difference between the one-stage (orange stars) and two-stage (blue x's) skill, but the two-stage skill drops as the error increases. Moreover, in the two-stage approach, for large RMSE/RMS_SSHA, there is a large spread between

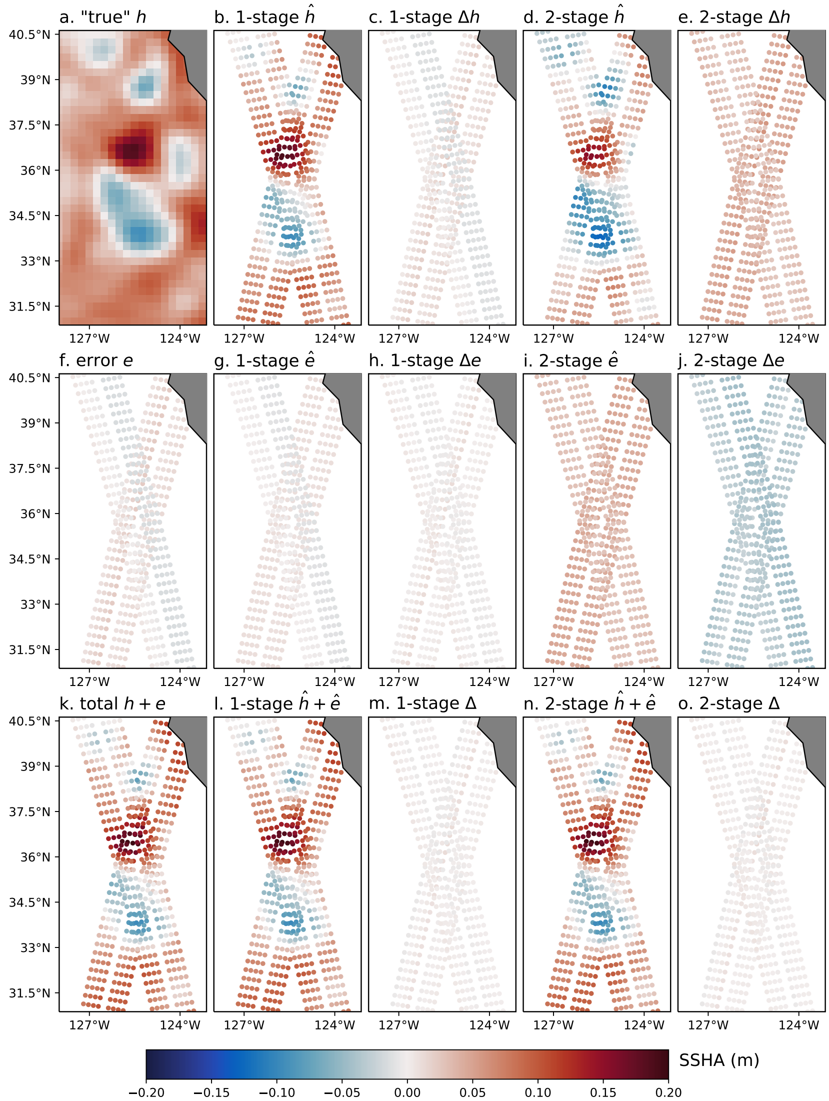

FIG. 5. SSHA $\mathbf{h}$ and uncertainties $\mathbf{e}$ (both in m) along SWOT satellite swath for 21 January 2016, showing, a) the "true" $\mathbf{h}$ derived by projecting gridded altimetry onto a set of Rossby waves. (Along-swath values are not shown but match the gridded values); b) $\hat{\mathbf{h}}_{1-stage}$ from the one-stage approach; c) $\mathbf{h} - \hat{\mathbf{h}}_{1-stage}$; d) $\hat{\mathbf{h}}_{2-stage}$ from the two-stage approach; e) $\mathbf{h} - \hat{\mathbf{h}}_{2-stage}$; f) correlated error $\mathbf{e}_{total}$ used in this simulation; g) estimated correlated error $\hat{\mathbf{e}}_{1-stage}$ from the one-stage approach; h) difference, $\Delta\mathbf{e} = \mathbf{e}_{total} - \hat{\mathbf{e}}_{1-stage}$; i) estimated error $\hat{\mathbf{e}}_{2-stage}$ from the two-stage approach; j) difference, $\Delta\mathbf{e} = e_{total} - \hat{\mathbf{e}}_{2-stage}$; k) total SSHA, $\mathbf{h} + \mathbf{e}_{total}$, used as input; l) total SSHA $\hat{\mathbf{h}} + \hat{\mathbf{e}}_{1-stage}$ from one-stage approach; m) difference between panels (k) and (l); n) total SSHA $\hat{\mathbf{h}} + \hat{\mathbf{e}}_{2-stage}$ from two-stage approach; o) difference between panels (k) and (n). In this case, $\mathbf{R} = \sigma_d^2\mathbf{I} = 0.01\mathbf{I}$, and the coefficients α_i have standard deviation 0.0125, with a resulting noise-to-signal ratio (root-mean-squared error divided by root-mean-squared signal) of 0.34.

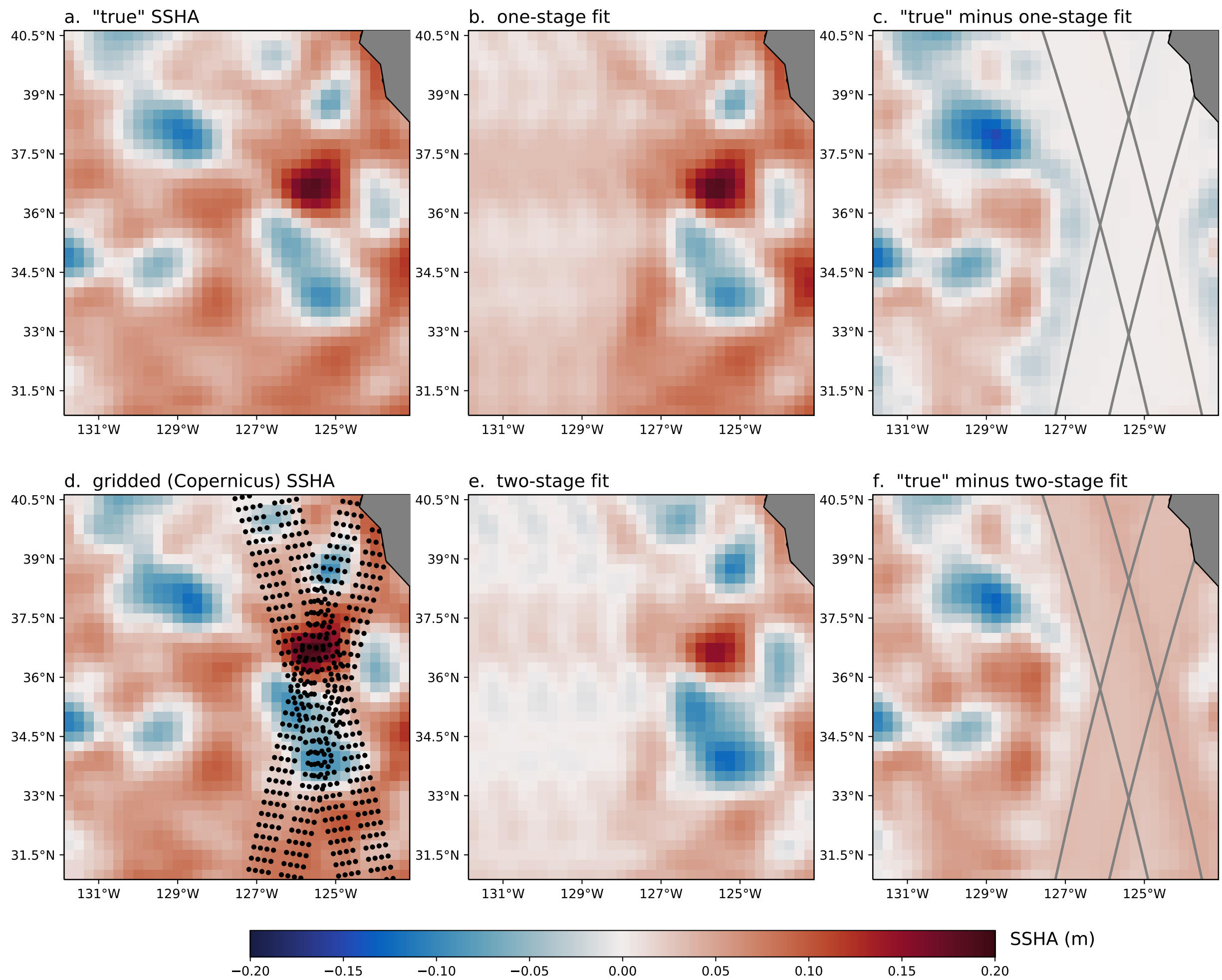

FIG. 6. a) The “true” SSHA on 21 January 2016, from a fitting process using 40 days of filtered data from 1 January 2016 through 9 February 2016; b) SSHA estimate of a 190-wave Rossby wave model in the one-stage approach; c) difference between true SSHA and estimated SSHA of one-stage approach, with black lines showing the center points of the outermost input data; d) The true/original SSHA on 1 January 2016; e) SSHA estimate of a 190-wave Rossby wave model in the two-stage approach; f) difference between true SSHA and estimated SSHA of two-stage approach. Noise-to-signal ratio is the same as in Figure 5.

the different ensemble members, indicating that the two-stage Rossby wave parameter estimation is less robust. For both the one-stage and two-stage approaches, correlated errors (Fig. 7b) are more accurately estimated when the error is large relative to the signal (larger RMSE/RMS_SSHA). Since we use the percentage variance explained as a skill metric, for small errors, the two-stage

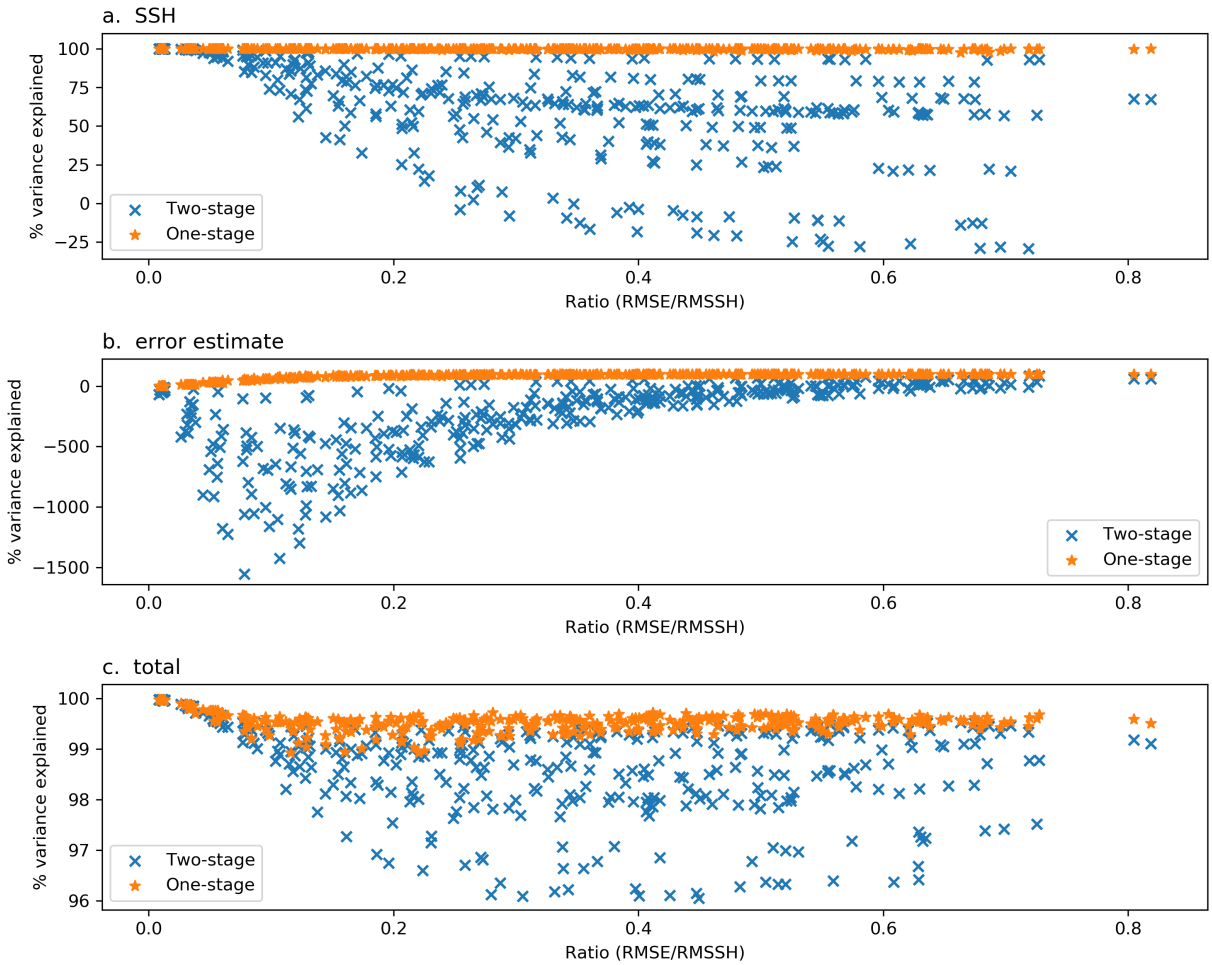

FIG. 7. (a) percentage variance explained in Sea Surface Height Anomaly (SSHA) estimate, (b) percentage variance explained in error estimate, and (c) percentage variance explained of the total input signal $\mathbf{h}+\mathbf{e}$, for the one-stage and two-stage approaches as a function of the ratio of root-mean-squared error to root mean squared SSHA, RMSE/RMS_SSHA ratio. In each plot, blue 'x' markers represent the two-stage approach, and orange '*' markers represent the one-stage approach.

approach can sometimes estimate errors that are unrelated to the "true" error, resulting in negative skill, while the one-stage approach consistently provides skillful error estimates.

Finally, since no random white noise is added to the observations, we expect that the fit should be able to fully reconstruct the combined SSHA and correlated error. As shown in Fig. 7c, this is indeed the case: the total "observed" signal, $\mathbf{h}_{swath} = \mathbf{h}+\mathbf{e}_{total}$, is well represented in both the one-stage and two-stage, with over 96% of the variance explained in all cases. The one-stage

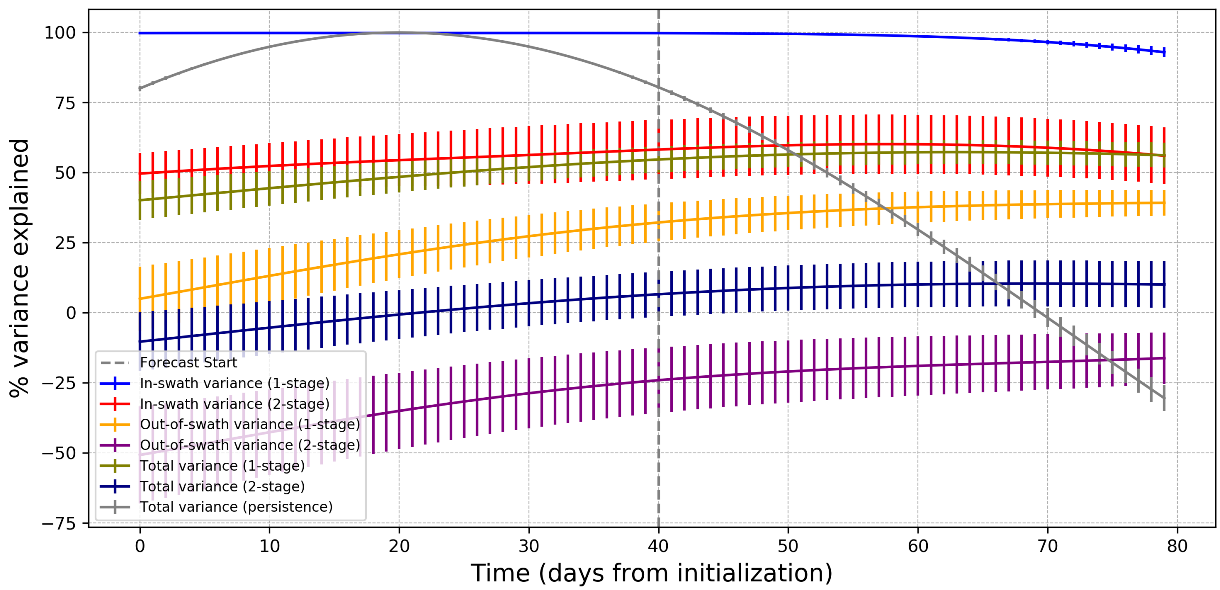

Fig. 8. Fraction of SSHA variance explained in one-stage and two-stage approaches, as a function of time, for in-swath only, out-of-swath only, and total domain, for correlated error with standard deviation 0.0125, as in Fig. 5. In this figure, model truth is determined from the gridded input fields, for example in Fig. 6a. The gray line indicates the skill that would be achieved by assuming persistence of conditions from the 21st day, here shown only for the full domain. All solid lines show ensemble statistics for 12 analysis start dates, beginning the first of each month in 2016. Error bars indicate one standard error of the mean. Gray dashed line indicates the 40-day mark when the forecast starts.

approach explains a slightly higher fraction of the overall variance; this is because this estimate has better prior information and fits all of the parameters simultaneously, which allows it to explain more of the normalized data variance for the same normalized model parameter cost.

The ensemble average of the fraction of variance explained illustrates the performance of both approaches (Fig. 8). In all parts of the domain and for all times, the one-stage approach performance is 20–30 percentage points better than the two-stage approach. Within the swath, the one-stage approach is able to explain almost all of the variance during the 40-day fitting period (blue line) and more than 90% of the variance in the 40-days after fitting. The two-stage approach explains more than 50% of the within-swath SSHA variance (red line). Outside the swath, skill increases noticeably over time as the Rossby waves propagate westward to fill in the full domain. In the one-stage approach the fraction of variance is consistently positive (gold line), while the two-stage approach initially shows negative skill outside the swath (purple line), consistent with no correlation between the fitted estimates and the "true" SSH. As we would expect, the fraction of variance explained for the full domain (green line for one-stage; dark blue for two-stage) is intermediate to the in-swath and out-of-swath results.

A standard benchmark is to compare forecast model performance against a baseline assumption of persistence—an assumption that conditions do not change relative to reference data. The gray line in Fig. 8 shows the skill achieved by persistence relative to the day 21 SSHA field (i.e. in this case the full gridded field that defines the "true" SSHA). The Rossby waves propagate slowly through the domain, so for short time separations, persistence is relatively skillful. Over longer time periods, the percent variance explained by persistence degrades quickly. By the end of the prediction period at day 80, both the one-stage and two-stage forecasts based on the Rossby-wave model show greater skill than persistence. (Keep in mind that these persistence results are expected to be show greater skill than if we had data only on the swath, with a guess of zero SSHA off swath.)

4. Conclusion

This study has aimed to provide a comprehensive analysis of the impact of roll error and other correlated errors on SWOT sea surface height (SSH) data assimilation. We have introduced a novel one-stage data assimilation approach that incorporates the process of correlated error reduction directly into the assimilation framework, contrasting with a two-stage methodology in which errors and ocean signals are analyzed separately. Our findings suggest that the one-stage approach enhances the robustness and accuracy of SSH estimates, especially in the presence of increasing correlated errors.

For demonstration purposes, we have used a simplified Rossby wave model to construct a clean data set capturing a leading-order pattern of SSHA variability in the California Current region. We then added spatially correlated noise to the filtered data and analyzed it using the same form of simplified Rossby wave model. This has allowed us to focus on the performance of the fit, without having to consider whether misfits were due to model shortcomings rather than noise in the SSHA.

Through a series of ensemble analyses, we varied the amplitude of the correlated errors and assessed their impact on SSHA estimation. The one-stage approach consistently outperformed the two-stage approach, particularly under conditions of high correlated error. While the two-stage approach showed diminished skill in estimating SSHA with increased levels of correlated error, the one-stage approach provided robust and skillful results, consistently explaining close to 100% of SSHA variance within the SWOT satellite swath, regardless of the error magnitude. Outside the satellite swath, the one-stage approach provides more skillful estimates of SSHA both during and after the fitting/assimilation time window. The skill in estimating correlated error terms is evaluated based on the fraction of variance explained. Large errors are more easily estimated than small errors since they represent a larger fraction of the total signal. Small errors can be difficult to estimate and therefore have large fractional uncertainties, but fortunately, since the errors are small, they have minimal impact on SSH.

Our results underscore the importance of addressing correlated errors as part of the data assimilation process. By doing so, we reduce the likelihood of misinterpreting instrument errors as ocean signals. SWOT Level 2 (L2) data have been released with guidelines for reducing or removing roll error, and an initial estimate of roll error has been removed from the Level 3 (L3) product produced by CLS. Nonetheless, L3 products have the potential to contain remnants of the correlated error that could be reduced using a one-stage assimilation approach.

In summary, our research demonstrates that for SWOT data assimilation an integrated one-stage approach that concurrently addresses correlated errors and ocean signal estimation has the potential to provide a reliable and robust representation of ocean dynamics. The approach documented in this paper is ready to be applied to actual SWOT data assimilation and could be extended to other types of correlated error, including for example the mean sea surface, offering the possibility of refining our representation of oceanic processes.

Acknowledgments. This study has been supported by the National Aeronautics and Space Administration (NASA) Surface Water and Ocean Topography (SWOT) Science Team, Award 80NSSC20K1136.

Data availability statement. Code for this project is available at https://github.com/sgille/swot_correlated_error or 10.5281/zenodo.11095818. . Data can be accessed via doi:10.5281/zenodo.10963448.

APPENDIX

Glossary

- $\mathbf{a}$: "true" model parameters
- $\hat{\mathbf{a}}$: best estimate of model parameters
- $\mathbf{a}_w$: Rossby wave model parameters
- $\mathbf{a}_{err}$: model parameters for correlated error terms
- B: buoyancy frequency
- c: phase speed of the first baroclinic Rossby wave
- D: depth of the water column
- $\mathbf{e}$: "true" correlated error, represented as a column vector
- $\hat{\mathbf{e}}$: best estimate of correlated error represented as a column vector
- f: Coriolis parameter
- $\mathbf{h}$: "true" or measured sea surface height, represented as a column vector
- $\hat{\mathbf{h}}$: best estimate of sea surface height measurements represented as a column vector
- $\tilde{\mathbf{h}}$: in two-stage method, sea surface height with estimated correlated error removed
- $\mathbf{H}$: model basis functions
- $H_{i,n}$, $H_{i,n+N_m}$: elements of Rossby waves expressed as cosines and sines, respectively.

- i: index for an observed SSHA measurement, at position $\mathbf{x}_i$ and time t_i
- k, l: zonal and meridional wavenumbers
- $\mathbf{k}$: vector wavenumber, with components defined by k and l
- L_d: first baroclinic Rossby wave deformation radius
- M: number of satellite swaths included; for daily data two passes per day
- N_g : the number of regularly gridded mapped SSHA values in the study domain, in this case 40 points in longitude by 36 points in latitude
- N_d : the number of SSHA observations input to the fitting procedure (defined by N_g to develop the simplified SSHA field and by N_s to test the one-stage and two-stage approaches)
- N_m: the number of waves included in the model
- N_s: the number of observations contained within the swath
- $\mathbf{P}$: $\sigma_w^2 I$, the portion of $\mathbf{P}_{total}$ representing the Rossby wave model parameters
- $\mathbf{P}_{err}$: the portion of $\mathbf{P}_{total}$ representing correlated error parameters
- $\mathbf{P}_{total}$: the covariance matrix representing prior uncertainty in all model parameters
- $\mathbf{r}$: residual
- $\mathbf{R}$: $\sigma_d^2 \mathbf{I}$, matrix represents the measurement (data) noise
- t_i: time of ith observation
- $\mathbf{x}_i$: geographic position in Cartesian coordinates
- α_0: timing error parameter,
- α_1: roll error parameter
- α_2: baseline dilation error parameter
- $\alpha_3, \alpha_4, \alpha_5, \alpha_6$: phase error parameters
- β: meridional derivative of the Coriolis parameter (df/dy)

- σ_d: standard deviation of the measurement (data) noise
- σ_w: standard deviation of the signal
- ω_n: frequency of Rossby waves

References

Chelton, D. B., and M. G. Schlax, 1996: Global observations of oceanic Rossby Waves. *Science*, **272 (5259)**, 234–238, https://doi.org/10.1126/science.272.5259.234.

Chelton, D. B., M. G. Schlax, and R. M. Samelson, 2011: Global observations of nonlinear mesoscale eddies. *Progress in Oceanography*, **91 (2)**, 167–216, https://doi.org/10.1016/j.pocean.2011.01.002.

Chelton, D. B., M. G. Schlax, R. M. Samelson, and R. A. de Szoeke, 2007: Global observations of large oceanic eddies. *Geophysical Research Letters*, **34 (15)**, https://doi.org/10.1029/2007GL030812.

Copernicus Marine Service Information, 2023: Global ocean gridded l4 sea surface heights and derived variables reprocessed 1993 ongoing. URL https://doi.org/10.48670/moi-00148, accessed: 2023-08-02, Marine Data Store (MDS), https://doi.org/10.48670/moi-00148.

Dibarboure, G., and C. Ubelmann, 2014: Investigating the performance of four empirical cross-calibration methods for the proposed swot mission. *Remote Sensing*, **6 (6)**, 4831–4869, https://doi.org/10.3390/rs6064831, URL https://www.mdpi.com/2072-4292/6/6/4831.

Dibarboure, G., and Coauthors, 2022: Data-driven calibration algorithm and pre-launch performance simulations for the SWOT Mission. *Remote Sensing*, **14 (23)**, 6070, https://doi.org/10.3390/rs14236070.

Esteban-Fernandez, D., 2017: SWOT project mission performance and error budget, revision a. Tech. rep., Jet Propulsion Laboratory.

Farrar, J. T., T. S. Durland, S. R. Jayne, and J. F. Price, 2021: Long-distance radiation of rossby waves from the equatorial current system. *Journal of Physical Oceanography*, **51 (6)**, 1947–1966, https://doi.org/10.1175/JPO-D-20-0048.1.

Fu, L.-L., D. Alsdorf, R. Morrow, E. Rodriguez, and N. Mognard, 2012: SWOT: The Surface Water and Ocean Topography Mission: Wide-Swath Altimetric Measurement of Water Elevation on Earth. Tech. Rep. 12-05, JPL, Jet Propulsion Laboratory, California Institute of Technology, Pasadena, California.

Fu, L.-L., and C. Ubelmann, 2014: On the transition from profile altimeter to swath altimeter for observing global ocean surface topography. *Journal of Atmospheric and Oceanic Technology*, **31 (2)**, 560–568, https://doi.org/10.1175/JTECH-D-13-00109.1.

Gaultier, L., C. Ubelmann, and L.-L. Fu, 2016: The challenge of using future SWOT data for oceanic field reconstruction. *Journal of Atmospheric and Oceanic Technology*, **33 (1)**, 119–126, https://doi.org/10.1175/JTECH-D-15-0160.1.

Gómez-Valdivia, F., A. Parés-Sierra, and A. L. Flores-Morales, 2017: Semiannual variability of the California Undercurrent along the Southern California Current System: A tropical generated phenomenon. *Journal of Geophysical Research*, **122 (2)**, 1574–1589, https://doi.org/10.1002/2016JC012350.

Ide, K., P. Courtier, M. Ghil, and A. C. Lorenc, 1997: Unified notation for data assimilation: Operational, sequential and variational; special issue: Data assimilation in meteology and oceanography: Theory and practice. *Journal of the Meteorological Society of Japan. Ser. II*, **75 (1B)**, 181–189, https://doi.org/10.2151/jmsj1965.75.1B_181.

Ivanov, L. M., C. A. Collins, T. M. Margolina, and V. N. Eremeev, 2010: Nonlinear Rossby waves off California. *Geophysical Research Letters*, **37**, L13 602, https://doi.org/10.1029/2010GL043708.

Kachelein, L., B. D. Cornuelle, S. T. Gille, and M. R. Mazloff, 2022: Harmonic analysis of non-phase-locked tides with red noise using the red tide package. *Journal of Atmospheric and Oceanic Technology*, **39 (7)**, 1031–1051, https://doi.org/10.1175/JTECH-D-21-0034.1.

Mazloff, M. R., B. Cornuelle, S. T. Gille, and J. Wang, 2020: The Importance of Remote Forcing for Regional Modeling of Internal Waves. *Journal of Geophysical Research: Oceans*, **125 (2)**, https://doi.org/10.1029/2019JC015623, URL https://onlinelibrary.wiley.com/doi/10.1029/2019JC015623.

Mazloff, M. R., S. T. Gille, and B. Cornuelle, 2014: Improving the geoid: Combining altimetry and mean dynamic topography in the California coastal ocean. *Geophysical Research Letters*, **41 (24)**, 8944–8952, https://doi.org/10.1002/2014GL062402.

Metref, S., E. Cosme, F. Le Guillou, J. Le Sommer, J.-M. Brankart, and J. Verron, 2020: Wide-swath altimetric satellite data assimilation with correlated-error reduction. *Frontiers in Marine Science*, **6**, 822, https://doi.org/10.3389/fmars.2019.00822.

Metref, S., E. Cosme, J. Le Sommer, N. Poel, J.-M. Brankart, J. Verron, and L. Gómez Navarro, 2019: Reduction of spatially structured errors in wide-swath altimetric satellite data using data assimilation. *Remote Sensing*, **11**, 1336, https://doi.org/10.3390/rs11111336.

Morrow, R., and Coauthors, 2019: Global observations of fine-scale ocean surface topography with the Surface Water and Ocean Topography (SWOT) Mission. *Frontiers in Marine Science*, **6**, 232, https://doi.org/10.3389/fmars.2019.00232.

Todd, R. E., D. L. Rudnick, M. R. Mazloff, R. E. Davis, and B. D. Cornuelle, 2011: Poleward flows in the southern California Current System: Glider observations and numerical simulation. *Journal of Geophysical Research*, **116**, C02 026, https://doi.org/10.1029/2010JC006536.

Wakata, Y., and S. Kitaya, 2002: Annual variability of sea surface height and upper layer thickness in the Pacific Ocean. *Journal of Oceanography*, **58**, 439–450, https://doi.org/10.1023/A:1021205129971.

Watanabe, W. B., P. S. Polito, and I. C. da Silveira, 2016: Can a minimalist model of wind forced baroclinic Rossby waves produce reasonable results? *Ocean Dynamics*, **66**, 539–548, https://doi.org/10.1007/s10236-016-0935-1.

Wunsch, C., 1996: *The Ocean Circulation Inverse Problem*. Cambridge University Press, Cambridge, 437 pp.